Editors' Suggestion

Unveiling the phase diagram of a bond-alternating spin-$\frac{1}{2}$ K-Γ chain

Qiang Luo [1], Jize Zhao [2,3,*], Xiaoqun Wang [4,5,†] and Hae-Young Kee [1,6,‡]

[1] *Department of Physics, University of Toronto, Toronto, Ontario M5S 1A7, Canada*

[2] *School of Physical Science and Technology & Key Laboratory for Magnetism and Magnetic Materials of the MoE, Lanzhou University, Lanzhou 730000, China*

[3] *Lanzhou Center for Theoretical Physics, Lanzhou University, Lanzhou 730000, China*

[4] *Key Laboratory of Artificial Structures and Quantum Control (Ministry of Education), School of Physics and Astronomy, Tsung-Dao Lee Institute, Shanghai Jiao Tong University, Shanghai 200240, China*

[5] *Beijing Computational Science Research Center, Beijing 100084, China*

[6] *Canadian Institute for Advanced Research, Toronto, Ontario, M5G 1Z8, Canada*

(Received 6 December 2020; accepted 1 April 2021; published 15 April 2021)

The key to unraveling intriguing phenomena observed in various Kitaev materials lies in understanding the interplay of Kitaev (K) interaction and a symmetric off-diagonal Γ interaction. To provide insight into the challenging problems, we study the quantum phase diagram of a bond-alternating spin-$\frac{1}{2}$ g_x-g_y K-Γ chain by density-matrix renormalization-group method where g_x and g_y are the bond strengths of the odd and even bonds, respectively. The phase diagram is dominated by even-Haldane ($g_x > g_y$) and odd-Haldane ($g_x < g_y$) phases where the former is topologically trivial while the latter is a symmetry-protected topological phase. Near the antiferromagnetic Kitaev limit, there are two gapped A_x and A_y phases characterized by distinct nonlocal string correlators. In contrast, the isotropic ferromagnetic (FM) Kitaev point serves as a multicritical point where two topological phase transitions meet. The remaining part of the phase diagram contains three symmetry-breaking magnetic phases. One is a sixfold degenerate FM_{U_6} phase where all the spins are parallel to one of the $\pm\hat{x}$, $\pm\hat{y}$, and $\pm\hat{z}$ axes in a six-site spin-rotated basis, while the other two have more complex spin structures with all the three spin components being finite. Existence of a rank-two spin-nematic ordering in the latter is also discussed.

DOI: 10.1103/PhysRevB.103.144423

I. INTRODUCTION

The enigmatic quantum spin liquid (QSL) has drawn a lot of attention ever since the seminal work of Anderson in 1973 [1]. In 2006, Kitaev proposed an exactly solvable spin-$\frac{1}{2}$ model on the honeycomb lattice and demonstrated that its ground state is an exotic QSL with emergent Majorana fermion excitations [2]. The past decade has witnessed a surge of interest in realization of the Kitaev honeycomb model on real materials with $4d$ or $5d$ magnetic ions, which includes iridates and α-$RuCl_3$ (see Refs. [3–5] and referees therein). However, because of the inevitable non-Kitaev interactions, e.g., the Heisenberg interaction and a symmetric off-diagonal exchange Γ interaction [6], these materials are shown to display magnetic orders at lowest temperatures [7–10]. Nevertheless, it is believed that the effective K-Γ model is the dominant ingredient to describe α-$RuCl_3$ [11].

From a theoretical point of view, although the quantum phase diagram of the K-Γ model on a honeycomb lattice is elusive, several magnetically ordered phases and distinct QSLs are demonstrated to exist [6,12–16], indicating the strong quantum fluctuation enhanced by competing interactions. Given the notorious difficulty in two dimension, it is beneficial and constructive to reduce the dimensionality where many full-fledged analytical and numerical methods capable of addressing problems in one-dimensional (1D) quantum spin chains are available. Recently, the phase diagram of the isotropic K-Γ chain has been studied by the density-matrix renormalization-group (DMRG) method and the non-Abelian bosonization technique [17,18]. It is shown that about 2/3 of the phase diagram is occupied by a gapless Luttinger liquid (LL). The ferromagnetic (FM) Kitaev limit is merely a transition point, while a critical segment near the antiferromagnetic (AFM) Kitaev limit is identified. Two symmetry-breaking phases termed the FM_{U_6} phase and the M_2 phase (see Fig. 2 for the nomenclature of the magnetically ordered phases) are also reported. Later on, it is found that FM and AFM Heisenberg interactions could open up a wide region of the FM_{U_6} phase and the LL, respectively [19]. However, how to enlarge the territory of the puzzling M_2 phase is still unclear. Aligning with this effort, a two-leg K-Γ ladder under a [111] magnetic field is also studied, revealing a rich phase diagram with several emergent phases [20].

Aside from the exotic phases and quantum criticality, quantum spin chains also provide an excellent platform for theoretical studies of various quantum phase transitions (QPTs) [21], of particular interest is the topological QPT that is beyond Landau's paradigm. The topological QPT occurs between two different phases without any explicit symmetry

*zhaojz@lzu.edu.cn
†xiaoqunwang@sjtu.edu.cn
‡hykee@physics.utoronto.ca

breaking [22–25]. The Haldane phase is such an example of symmetry-protected topological (SPT) phase [26], which possesses a nonlocal string order parameter (SOP) due to a hidden $\mathbb{Z}_2 \times \mathbb{Z}_2$ symmetry breaking [27,28]. Dating back to 1992, Hida originally pointed out that the bond-alternating spin-$\frac{1}{2}$ Heisenberg chain could host the Haldane phase due to the imbalance of the neighboring coupling intensities, leading to the formation of either total spin 0 or 1 out of the two spin-$\frac{1}{2}$ degrees of freedom [29]. Therefore, bond alternation is a practical route to legalize the validity of the SPT phase in spin-$\frac{1}{2}$ chains [30]. We also note that the anisotropic Kitaev spin chain hosts two disordered phases which undergo a direct transition at the isotropic point [31,32]. These observations motivate us to investigate the ground-state properties of the K-Γ chain by altering the bond strength of adjacent sites.

In this paper, we study the phases and QPTs of a bond-alternating $S = \frac{1}{2}$ K-Γ chain. When $\Gamma = 0$, it is the Kitaev spin chain, otherwise known as the exactly solvable 1D quantum compass model (QCM) [31,32]. Beyond that it is nonintegrable except for some special points and lines when $|K| = |\Gamma|$. Therefore, we resort to the DMRG method [33–35] to map out the quantum phase diagram. The phase boundaries are determined by various quantities including the energy gap and entanglement entropy. The central charge is calculated to distinguish the universality class of a continuous QPT.

The structure of the paper is as follows: In Sec. II we introduce the theoretical model under investigation, analyze the symmetry properties, and present the phase diagram of interest. Following this, we study two topological QPTs in Secs. III and IV. Section V presents the magnetic order parameters of symmetry-breaking phases. In Sec. VI we study the transitions between the left and right panels of the phase diagram. We conclude with a summary in Sec. VII. Finally, a brief review of the diagonalization of QCM and some other useful contents are presented in the Supplemental Material [36].

II. MODEL AND METHOD

We consider a bond-alternating spin-$\frac{1}{2}$ K-Γ chain with

$$\mathcal{H} = \sum_{l=1}^{L/2} g_x \mathcal{H}^{(x)}_{2l-1,2l}(\theta) + g_y \mathcal{H}^{(y)}_{2l,2l+1}(\theta), \tag{1}$$

where L is the chain length, g_x (g_y) is the odd (even) bond strength, and

$$\mathcal{H}^{(\gamma)}_{i,j}(\theta) = K S^\gamma_i S^\gamma_j + \Gamma\left(S^\alpha_i S^\beta_j + S^\beta_i S^\alpha_j\right). \tag{2}$$

Here, K and Γ are the Kitaev interaction and the off-diagonal exchange interaction, respectively. γ could be either x or y and it specifies the spin direction associated with the referred bond, see Fig. 1(a). For each γ bond, α and β are the two remaining mutually exclusive spin directions. In what follows we parametrize $K = \sin\theta$ and $\Gamma = \cos\theta$ with $\theta \in (-\pi, \pi]$.

Before carrying out numerical calculation, let us analyze the symmetries in the parameter space which will reduce the computational cost. Akin to the transverse-field Ising model [37], the model (1) owns a duality relation which could be seen by applying the spin rotation transformation $(S^x_i, S^y_i, S^z_i) \to (-S^y_i, -S^x_i, -S^z_i)$. This implies that each

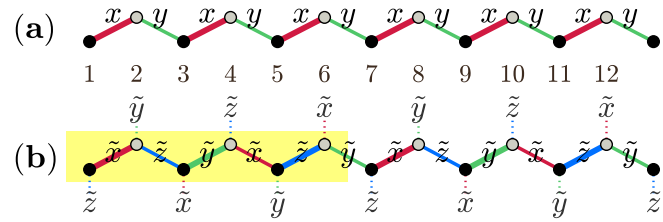

FIG. 1. (a) Sketch of the bond structure in the original form. Here, x (red) and y (green) stand for the γ index and the width is proportional to the bond strength. (b) Pictorial bond structure of the Hamiltonian in the rotated basis. The overhanging bond at each site is determined by the remaining one along the chain. The shaded region represents the six-site unit cell.

eigenvalue E of H satisfies the relation

$$E(g) = gE(1/g), \tag{3}$$

where $g \equiv g_y/g_x$ is the relative bond strength. On the other hand, by virtue of a global spin rotation around the z axis by π, $(S^x_i, S^y_i, S^z_i) \to (S^y_i, -S^x_i, S^z_i)$, the Kitaev interaction remains uninfluenced whereas the sign of the Γ interaction is altered [17]. We thus instantly find that

$$E(K, \Gamma) = E(K, -\Gamma), \tag{4}$$

or, equivalently, $\theta \mapsto \pi - \theta$. These relations in Eq. (3) and Eq. (4) allow us to focus on the phase diagram primarily in the reduced parameter range $\theta \in [-\pi/2, \pi/2]$ and $g = g_y/g_x \in [0, 1]$ and then map out the whole phase diagram shown in Fig. 2.

Using a site-ordering cross decimation rotation with a periodicity of six sites, all the cross terms of $S^\alpha_i S^\beta_j$ with $\alpha \neq \beta$ in Eq. (2) will vanish [17]. This U_6 transformation is given by

$$\begin{aligned}
&\text{sublattice 1} : (x, y, z) \to (\tilde{x}, \tilde{y}, \tilde{z}),\\
&\text{sublattice 2} : (x, y, z) \to (-\tilde{x}, -\tilde{z}, -\tilde{y}),\\
&\text{sublattice 3} : (x, y, z) \to (\tilde{y}, \tilde{z}, \tilde{x}),\\
&\text{sublattice 4} : (x, y, z) \to (-\tilde{y}, -\tilde{x}, -\tilde{z}),\\
&\text{sublattice 5} : (x, y, z) \to (\tilde{z}, \tilde{x}, \tilde{y}),\\
&\text{sublattice 6} : (x, y, z) \to (-\tilde{z}, -\tilde{y}, -\tilde{x}),
\end{aligned} \tag{5}$$

where γ [$=x(\tilde{x})$, $y(\tilde{y})$, $z(\tilde{z})$] denotes the spin component of S^γ ($\tilde{S}^\gamma$). Under this transformation the original Hamiltonian acquires the following form [17]:

$$\tilde{\mathcal{H}}^{(\gamma)}_{i,j}(\theta) = -K\tilde{S}^\gamma_i \tilde{S}^\gamma_j - \Gamma\left(\tilde{S}^\alpha_i \tilde{S}^\alpha_j + \tilde{S}^\beta_i \tilde{S}^\beta_j\right), \tag{6}$$

in which the bonds $\gamma = \tilde{x}$ (red), $\tilde{z}$ (blue), and $\tilde{y}$ (green) circularly, as depicted in Fig. 1(b). $\tilde{\mathbf{S}} = (\tilde{S}^x_i, \tilde{S}^y_i, \tilde{S}^z_i)$ is the spin operator in the rotated basis. Such a U_6 transformation does not alter the energy spectra (i.e., energy and its degeneracy) but simplifies the spin-spin correlation functions. Therefore, we will preferentially focus on the rotated Hamiltonian in Eq. (6) unless stated explicitly otherwise. The exceptions are Secs. IV and VI, where it is convenient to calculate the correlation functions in the original basis. In addition, combining Eq. (4), it is apparent that Eq. (6) has an SU(2) symmetric structure when $|K| = |\Gamma|$. Specifically, in the range

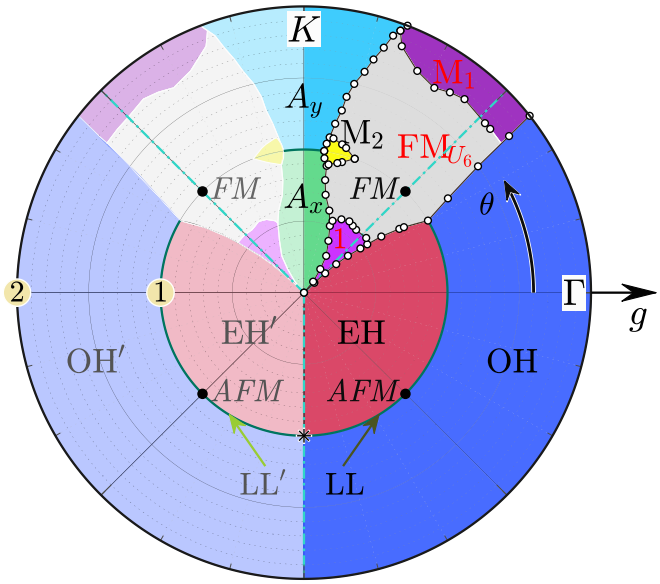

FIG. 2. Quantum phase diagram of the bond-alternating spin-$\frac{1}{2}$ K-Γ chain with $K = \sin\theta$ and $\Gamma = \cos\theta$. The green thick line marked by *circled*1 is the isotropic K-Γ chain, and the black solid circles at $\theta = \pi/4$ and $-\pi/4$ represent the hidden SU(2) FM and AFM Heisenberg chains, respectively. The asterisk ($*$) in the vertical line represents a multicritical point. There are seven distinct phases in the right panel which are the main focus of the paper. The EH-OH transition and A_x-A_y transition are continuous with a central charge of $c = 1$ and $\frac{1}{2}$, respectively. The nature of the magnetically ordered states, the FM_{U_6} phase, the M_1 phase, and the M_2 phase, are clarified in a six-site U_6 rotated basis. See the main text for details.

$\theta \in [-\pi/2, \pi/2]$, the point $\theta = -\pi/4$ and $\pi/4$ corresponds to an AFM and FM Heisenberg chain, respectively.

The numerical calculations are performed by the DMRG method [33–35], which is a powerful technique for 1D many-body problems. Periodic boundary conditions (PBCs) are preferred to weaken the finite-size effect and open boundary conditions (OBCs) are also adopted occasionally for comparison. We keep up to 2000 states so as to ensure a typical truncated error of $\approx 10^{-7}$ or less. The chain length L is strictly considered to be the multiple of six, consistent with the structure of the unit cell and the U_6 transformation.

The resultant phase diagram is shown in Fig. 2, which has a salient feature of mirror (left-right) symmetry. Focusing on the right half circle, it harbours *seven* distinguishing phases. Four of them, i.e., the even-Haldane (EH) and odd-Haldane (OH) phases and the A_x and A_y phases [2], are disordered and could be characterized by nonlocal SOPs of different kinds. The rest are three magnetically ordered phases named the FM_{U_6} phase and the M_1 and M_2 phases. The FM_{U_6} phase is collinear in the rotated basis and exhibits sixfold degeneracy. The M_1 and M_2 phases show more complex spin patterns where all three spin components are finite. For the M_1 phases, it is stabilized at the region where $g \lesssim 1/\sqrt{3}$ or $g \gtrsim \sqrt{3}$ and *one* of the spin components is dominantly the biggest. For the M_2 phases, it locates around the very isotropic line of $g \simeq 1$ where $K/\Gamma > 1$ and *two* of its spin components are almost the same and is larger than the third.

III. EVEN-HALDANE–ODD-HALDANE TOPOLOGICAL QUANTUM PHASE TRANSITION

Straightforwardly, when $\theta = -\pi/4$, Eqs. (1) and (6) turn out to be a bond-alternating AFM Heisenberg chain [29,38–41]. It is well-established that there is a topological EH-OH transition at $g = 1$ with a central charge $c = 1$ [40]. For either $g < 1$ or $g > 1$, the ground state could be characterized by a SOP which is nonzero inside the phase but vanishes otherwise (see Sec. II in the Supplemental Material [36]). Specifically, the two phases could be distinguished by the even- and odd-SOPs which are defined as [29]

$$\mathcal{O}_e^\alpha = \lim_{|j-i|\to\infty} \mathcal{O}^\alpha(2i, 2j+1), \tag{7}$$

and

$$\mathcal{O}_o^\alpha = \lim_{|j-i|\to\infty} \mathcal{O}^\alpha(2i-1, 2j), \tag{8}$$

where

$$\mathcal{O}^\alpha(p,q) = -4\left\langle \tilde{S}_p^\alpha \left(\prod_{p<r<q} e^{i\pi \tilde{S}_r^\alpha} \right) \tilde{S}_q^\alpha \right\rangle. \tag{9}$$

Here, $\alpha = x, y, z$. The even-SOP $\mathcal{O}_e^\alpha$ is calculated from an even site $(2i)$ to an odd site $(2j+1)$ while the odd-SOP $\mathcal{O}_o^\alpha$ is measured from an odd site $(2i-1)$ to an even site $(2j)$. At the critical point $g = 1$, both SOPs are identical and decay as $\mathcal{O}_{e/o} \sim L^{-1/4}$ [42]. From a topological perspective, the EH phase is trivial while the OH is a SPT phase which is isomorphic to the ground state of the spin-1 Heisenberg chain [24]. For the OH phase, its ground state is unique under PBC but has a fourfold degeneracy under OBC because of two edge spin $\frac{1}{2}$s. In addition, the degeneracy of the lowest-lying entanglement spectrum is twofold (fourfold) under OBC (PBC) [43].

As shown in Fig. 2, the EH and OH phases extend to a large region of the parameter space. To demonstrate it, we focus on the line of $\theta = 0$, which is the Γ-chain limit. We begin by studying a so-called *bulk entanglement gap* $\Delta\mathcal{S}$ [44], which comes from the even-odd oscillation of the entanglement entropy $\mathcal{S}_L(l) = -\mathrm{Tr}(\rho_l \ln \rho_l)$ where ρ_l is the reduced density matrix of the subsystem with a contiguous spatial segment l [45]. Depending on whether $l \gg 1$ is odd or even, $\mathcal{S}_L(l)$ saturates to a constant value of $\mathcal{S}_1$ and $\mathcal{S}_2$, respectively. The bulk entanglement gap is thus defined as $\Delta\mathcal{S} = \mathcal{S}_2 - \mathcal{S}_1$ [44]. Figure 3(a) shows $\mathcal{S}_1$ (open symbols) and $\mathcal{S}_2$ (fill symbols) for the chain length $L = 48$, 96, and 144. For these lengths chosen, $\mathcal{S}_1$ corresponds to cut one strong valence bond consistently, while $\mathcal{S}_2$ stands for cutting a strong valence bond zero time or twice when $g < 1$ or $g > 1$, respectively. This implies that the bulk entanglement gap $\Delta\mathcal{S}/\ln 2$ tends to be -1 or 1 in the limiting case where $g \to 0$ or $g \to \infty$, respectively [see Fig. 3(b)]. Near the critical point, $\mathcal{S}_1 \simeq \mathcal{S}_2$ and thus $\Delta\mathcal{S} \simeq 0$. Moreover, defining $\delta = \frac{g-1}{g+1}$, the quantity scales as $\Delta\mathcal{S} \sim \ln 2 - (1-|\delta|)^2$ when away from criticality, whereas $\Delta\mathcal{S} \sim -\delta \ln|\delta|$ when close to criticality [44]. Therefore, the value of $\Delta\mathcal{S}$ is bounded to $\pm \ln 2$ and its sign $W = \mathrm{sgn}(\Delta\mathcal{S})$ could be used to characterize the corresponding topological sector. The sign change (e.g., from $W = -1$ to 1) is a signal for the topological QPT.

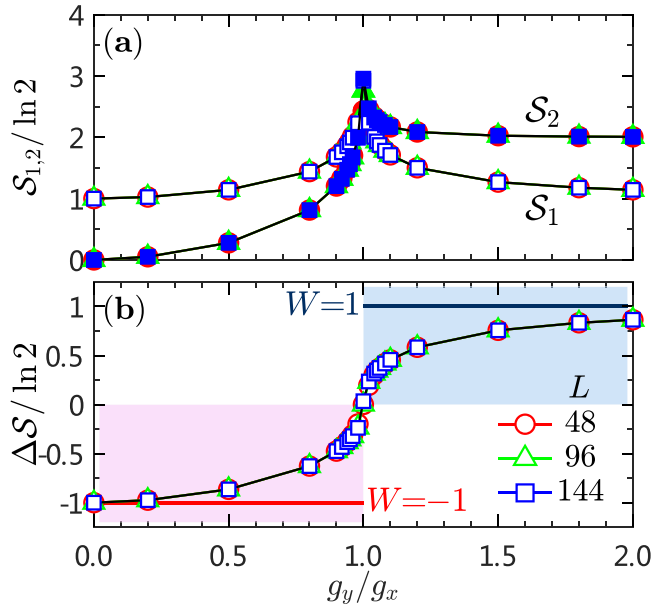

FIG. 3. (a) Entanglement entropy $\mathcal{S}_1$ (open symbols) and $\mathcal{S}_2$ (filled symbols) of different cuts for the g_x-g_y Γ chain with $\theta = 0.00\pi$. The chain length L is 48 (red circles), 96 (green triangles), and 144 (blue squares). (b) Bulk entanglement gap $\Delta\mathcal{S}$ in the same region as in panel (a). $W = -1$ and 1 are the sign of $\Delta\mathcal{S}$ when $g < 1$ and $g > 1$, respectively.

To further reveal the nature of phases at different topological sectors, we measure the even-SOP $\mathcal{O}_e^z$ [see Eq. (7)] and odd-SOP $\mathcal{O}_o^z$ [see Eq. (8)]. It is clearly shown in Fig. 4(a) that $\mathcal{O}_e^z$ ($\mathcal{O}_o^z$) is finite when $g < 1$ ($g > 1$) and is vanishingly small

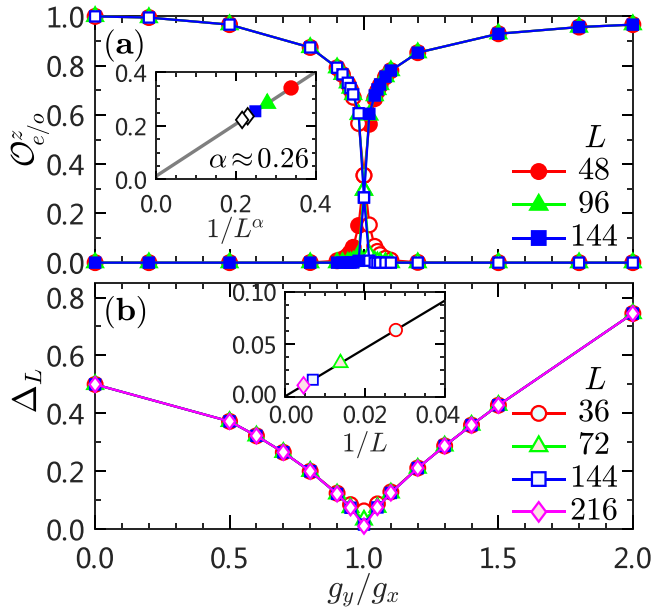

FIG. 4. (a) SOPs of the even type $\mathcal{O}_e^z$ (open symbols) and odd type $\mathcal{O}_o^z$ (filled symbols) for the g_x-g_y Γ chain with $\theta = 0.00\pi$. The inset shows the asymptotic decay of SOP $\mathcal{O}$ at $g_x = g_y$. (b) Energy gap Δ_L in the same region as in panel (a). Inset shows the linear extrapolation of the energy gap at $g_x = g_y$.

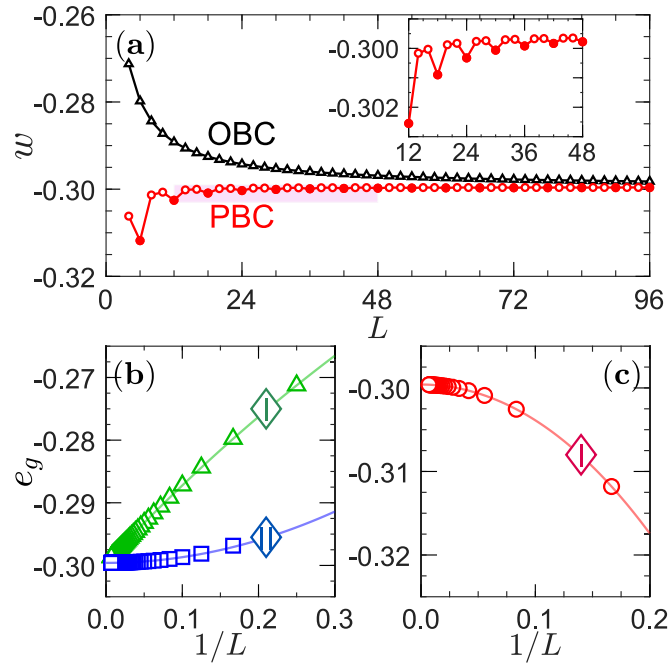

FIG. 5. (a) Behavior of the energy density $w = E_g(L)/L$ for the isotropic Γ chain under OBC (black) and PBC (red). The inset shows the six-site periodicity of w under PBC. Panels (b) and (c) show the estimate of e_g for the isotropic Γ chain under OBC and PBC, respectively. The roman numerals I (green and red) and II (blue) mark two different methods illustrated in the text.

otherwise. The finite-size effects of $\mathcal{O}_e^z$ and $\mathcal{O}_o^z$ are very weak, except for a narrow window that is close to the critical region. As shown in the inset, both types of SOPs $\mathcal{O}_e^z$ and $\mathcal{O}_o^z$ decay algebraically as $L^{-\alpha}$ where the critical exponent $\alpha \approx 0.26$, which is fairly close to the value of 1/4 at $\theta = -\pi/4$ [42]. For an infinite-size system, SOPs $\mathcal{O}_e^z$ and $\mathcal{O}_o^z$ scale as $\delta^{1/6}$ [29]. As a result, the critical exponent is given as $\beta = 1/12$ because $\mathcal{O} \propto \delta^{2\beta}$. Hence, this topological QPT belongs to the Gaussian universality class. We also calculate the excitation gap Δ_T, which is defined as the energy difference between the first-excited state and the ground state. Figure 4(b) shows that Δ_T is very robust when $g \neq 1$. Near $g = 1$, it has a pronounced drop with size increased. As shown in the inset, Δ_T is zero when $L \to \infty$, showing that the ground state of the isotropic Γ chain is critical. To extract the central charge c, we calculate the von Neumann entanglement entropy $\mathcal{S}_L(L/2)$ for a series of chain length L and the central charge is fit by $\mathcal{S}_L = \frac{c}{3}\ln(L/\pi) + c'$. Our best fitting suggests that $c \simeq 0.997(5)$ (not shown), which is very close to 1 of the LL.

Figure 5(a) displays the energy density E_g/L of the isotropic Γ-chain under OBC (black triangles) and PBC (red circles). For the OBC case, E_g/L decreases smoothly and saturates around -0.30 as L increases. In contrast, it is not monotonically increasing but exhibits an oscillation with six-site periodicity for the PBC (see inset). As a comparison, we note that such an abnormal energy density behavior is absent in the isotropic Kitaev spin chain (see Fig. 1 in the Supplemental Material [36]). This phenomenon in the Γ chain is striking and may be related to the unusual energy behavior of the Γ model on the honeycomb lattice [15]. In Ref. [15]

the total energy E_g is calculated on a series of honeycomb clusters where OBC (PBC) is utilized on the L_x (L_y) direction of cylinders. For any cylinder with fixed L_y, the energy density E_g/N ($N = L_xL_y$) varies linearly with $1/L_x$. However, by increasing the circumference of the cylinders with $L_x/L_y = 2$, the energy density E_g/N is no longer monotonic and exhibits a skew sawtooth behavior.

To round off the calculation, we give an estimate of the ground-state energy per-site e_g of the isotropic Γ chain. We note that our Γ chain contains both x and y bonds [see Eq. (1)], and there is no analytical solution so far. It is fundamentally different from a z-bond Γ chain which could be solved exactly via the Jordan-Wigner transformation [46]. At the quantum critical point, the finite-size scaling of the ground-state energy $E_g(L)$ is known to be [47,48]

$$E_g(L) = Le_g + \varepsilon_b - \frac{\Delta_b}{L} + O(L^{-2}), \tag{10}$$

where e_g is the average bulk energy per-site, ε_b is the size-independent surface energy which vanishes in the case of PBC, and Δ_b is the subleading correlation term. It is found that $\Delta_b = \pi c/6$ ($\pi c/24$) for PBC (OBC) where c is the central charge [47,48]. By definition we have $e_g = \lim_{L\to\infty} e_L$ where e_L is the energy per-site of the chain with length L. For the energy obtained under the OBC, there are two ways to extrapolate it to the thermodynamic limit; one is $e_L^{\mathrm{I}} = E_g(L)/L$ and the other is $e_L^{\mathrm{II}} = [E_g(L) - E_g(L-2)]/2$. It is easy to check that convergence speed of the latter is faster than the former. As shown in Fig. 5(b), the quadratic fittings of the two give that $e_g^{\mathrm{I}} = -0.299\,593\,62$ and $e_g^{\mathrm{II}} = -0.299\,593\,75$, yielding an estimate for the ground-state energy per-site in the thermodynamic limit of $e_g = -0.299\,593\,7(1)$ with seven significant digits. Meanwhile, we also extrapolate the energy under PBC by using the solid points in Fig. 5(a) where L is a multiple of six [see Fig. 5(c)]. Our result suggests that $e_g \approx -0.299\,594$, which is fairly consistent with the high-precision value revealed by the calculation under OBC.

IV. EXTENDED QUANTUM COMPASS MODEL

In the absence of the Γ interaction, Eqs. (1) and (2) are reduced to the 1D Kitaev spin chain, which is also known as the 1D QCM in some other contexts [31,32]. The QCM could be solved exactly by Jordan-Wigner transformation, and its dispersion relation is almost the same as that of the transverse-field Ising model. There is a topological QPT between the gapped A_x and A_y phases at $g = 1$ [2]. However, because of intermediate symmetries, the ground state of the QCM possesses a huge number of degeneracy $2^{N/2-1}$ ($2^{N/2}$) under PBC (OBC) where N is the total number of sites [31,49]. Equivalently, the QCM could be rewritten as a Majorana fermion chain complemented by N decoupled Majorana fermions. Since each Majorana fermion has $\sqrt{2}$ degrees of freedom, the redundant Majorana fermions thus contribute a ground-state degeneracy of $O(2^{N/2})$ [50]. These degenerate ground states are vulnerable and can be totally lifted by an infinitesimal transverse field [51]. The entanglement [52–55], energy dynamics [56], and the dissipative behavior [57] of the QCM have been studied over the years.

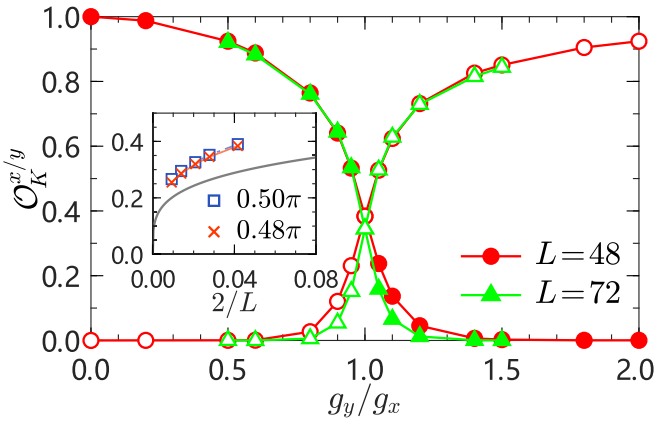

FIG. 6. Kitaev-type SOP $\mathcal{O}_K^{x/y}$ of the g_x-g_y K-Γ chain for $\theta = 0.48\pi$ with chain length $L = 48$ (red circles) and 72 (green triangles). The inset shows the behavior of $\mathcal{O}_K^x$ at the isotropic point $g = 1$. Values at $\theta = 0.50\pi$ (blue squares) and $\theta = 0.48\pi$ (red cross) are shown for several chain lengths $L = 48$, 72, 96, 144, and 216. The sold line is the correlation function defined in Eq. (13).

Using the spin duality transformation, the topological A_x and A_y phases, respectively, are shown to possess nonlocal string correlators [50],

$$\mathcal{O}_K^x(2r) = \lim_{r\to\infty} \left\langle \prod_{k=1}^{2r} \sigma_k^x \right\rangle \tag{11}$$

and

$$\mathcal{O}_K^y(2r) = \lim_{r\to\infty} \left\langle \prod_{k=2}^{2r+1} \sigma_k^y \right\rangle, \tag{12}$$

where σ_k^x and σ_k^y are Pauli matrices, i.e., twice the spin-$\frac{1}{2}$ operators in the *original* basis. Here, the nonlocal SOPs are defined in the original basis embedded in Eq. (2). Generalization of nonlocal SOPs to a two-leg Kitaev ladder has been discussed in a recent work [58]. At the critical point $g = 1$, these Kitaev-type SOPs vanish in an algebraic behavior at long-distance limit $n \gg 1$ [37],

$$\mathcal{O}_K^{x/y}(n) = e^{1/4}2^{1/12}A^{-3}n^{-1/4}\left(1 - \tfrac{1}{64}n^{-2} + \cdots\right), \tag{13}$$

where $A \simeq 1.2824$. For infinite-size case, they obey a scaling law and $\mathcal{O}_K^x \sim (1-g^2)^{1/4}$ when $g \to 1^-$.

Hereafter we show numerically that the topological A_x and A_y phases are extended when θ is slightly deviated from $\pi/2$ (AFM Kitaev point). We demonstrate this by calculating the SOPs shown in Eqs. (11) and (12) for $\theta = 0.48\pi$ with $2r = L/2$. As presented in Fig. 6, the SOPs change smoothly and are very robust in each corresponding phase, showing the validity of them in this region. When $g = 1$, the two have the same value due to the self-dual relation and they decrease visibly as L grows. To measure how the SOPs vary at this point, we calculate $\mathcal{O}_K^x$ for L up to 216 sites and the results are shown in the inset. The values at $\theta = 0.50\pi$ are also shown for comparison. As revealed by Eq. (13), the leading term of $\mathcal{O}_K^x$ is $\sim 1/L^{1/4}$, so its decay ratio is not very rapid for modest chain length L as shown by the solid line in the inset. However, it is constructive to note that $\mathcal{O}_K^x$ at $\theta = 0.48\pi$ and 0.50π are very

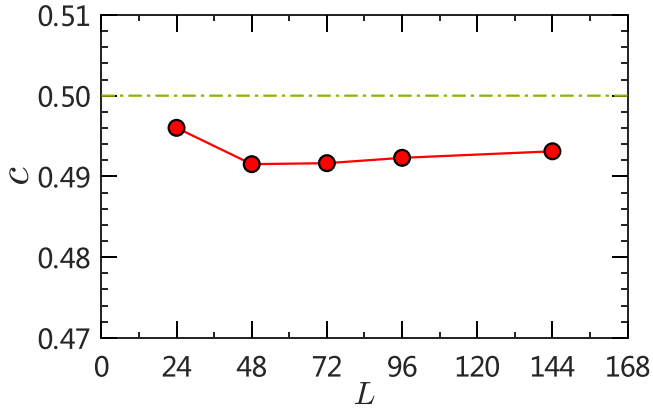

FIG. 7. Estimate of the central charge c for the critical K-Γ chain at $(g = 1.00, \theta = 0.48\pi)$.

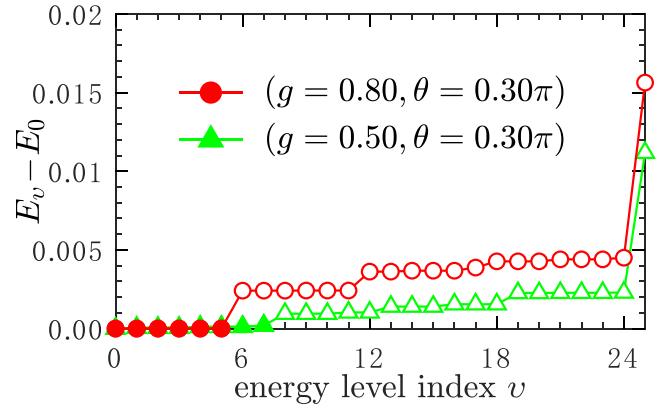

FIG. 8. Low-lying energy levels E_υ for $\theta = 0.30\pi$ with chain length $L = 24$. The ground-state degeneracy is sixlet and octuplet for $g = 0.80$ (red circles, FM_{U_6} phase) and $g = 0.50$ (green triangles, M_1 phase), respectively.

close but the curve of $\theta = 0.48\pi$ is shifted downward slightly when compared with the latter. For $\theta = 0.50\pi$ it is known that $\mathcal{O}_K^x$ vanishes at $g = 1$ when $L \to \infty$ [50]. So it is reasonable for us to believe that it will also go to zero ultimately for $\theta = 0.48\pi$. As a result, $g = 1$ is still inferred as the critical point for the A_x-A_y transition.

To confirm the criticality at $\theta = 0.48\pi$, we now turn to calculate the central charge. The central charge is usually extracted from the coefficient of the logarithmic correlation in the entanglement entropy [45]. However, this method is not optimal for the critical Kitaev phase because of the macroscopic ground-state degeneracy [31]. As a result, it is challenging to get a minimally entangled state which is essential for a reliable estimate of the central charge. The practical way to handle this problem is by the energy scaling as shown in Eq. (10). For the PBC, the central charge is given by the following formula:

$$c_L \simeq \frac{6}{\pi}[Le_g - E_g(L)]L, \tag{14}$$

where e_g is the only relevant parameter. Following a similar procedure illustrated in Fig. 5(b), we find $e_g \approx -0.159\,109\,2$ for $\theta = 0.48\pi$, which is only slightly larger than that of $-1/(2\pi) = -0.159\,154\,9\cdots$ for $\theta = \pi/2$. We have also calculated the ground-state energy $E_g(L)$ for a series of chain length L ranging from 24 to 144. The fitting central charge via Eq. (14) is shown in Fig. 7. It can be found that the central charge is very close to $\frac{1}{2}$ and suffers from a tiny finite-size effect. Therefore, we draw the conclusion that the central charge $c = \frac{1}{2}$ and the transition belongs to the same universality class as that at $\theta = \pi/2$ [59,60], confirming the existence of an extended region of A_x and A_y phases and the critical transition line between them.

V. THE SYMMETRY-BREAKING PHASES

A. Degeneracy and spin patterns

Like the AFM case shown in Sec. III, Eqs. (1) and (6) could be reduced to the bond-alternating FM Heisenberg chain when $\theta = \pi/4$ (i.e., $K = \Gamma$). For this model its ground-state energy $E_g = -(1+g)KL/8$ with a $(L+1)$-fold ground-state degeneracy [61]. Although it is inherently gapless, the system is not conformally invariant. Specially, when $g = 1$ it is shown that there is an effective central charge $c_{\mathrm{eff}} = 3/2$ [62]. Around the isotropic SU(2) FM point by tuning θ along the line of $g = 1$, there is an $O_h \to D_4$ symmetry-breaking phase which has sixfold degenerate ground states along the $\pm\hat{x}$, $\pm\hat{y}$, and $\pm\hat{z}$ spin directions [17]. In addition, the local magnetization, say $\langle\tilde{S}_i^z\rangle$, shows a three-site periodicity where two of them are equal,

$$\langle\tilde{\mathbf{S}}_1\rangle = c\hat{z}, \quad \langle\tilde{\mathbf{S}}_2\rangle = a\hat{z}, \quad \langle\tilde{\mathbf{S}}_3\rangle = a\hat{z}, \tag{15}$$

in which a and c are the strengths of the local magnetization. With the U_6 transformation shown in Eq. (5) in mind, it is easy to check that spins in the original basis are $(|S_1^z|, |S_2^y|, |S_3^y|; |S_4^z|, |S_5^x|, |S_6^x|) = (c, a, a; c, a, a)$. The inherent frustration in model (6) is accidentally eliminated when $\theta = \pi/4$. Away from this line, the interplay of bond anisotropy and competing interactions would enhance quantum fluctuations, giving rise to new type of magnetic orderings. It is shown in Fig. 2 that there are three distinct magnetically ordered states in the middle area where one is a collinear FM_{U_6} phase while the other two are dubbed M_1 and M_2 phases.

To begin with, by reducing the strength of g along the line of $\theta = 0.30\pi$, we find that FM_{U_6} phase could survive until $g \simeq \sqrt{3}/3$ where the ground-state degeneracy changes from sixlet to octuplet. Figure 8 show the first $(L+2)$ energy levels E_υ $(\upsilon = 0 \to 25)$ of a 24-site chain at $g = 0.80$ (red circles) and 0.50 (green triangles). One can readily recognize that there is a energy step at the sixth (eighth) energy level for $g = 0.80$ (0.50). The energy barrier is $\approx 10^{-3}$, which is several orders larger than the energy splitting within the degenerate ground states. The energy step at the 24th energy level is extremely steep, which is a reminiscence of the $(L+1)$-fold degeneracy at the SU(2) FM line of $\theta = \pi/4$. We have checked the ground-state degeneracies under spin chains of $L = 48$ and 72 as well, and the results remain unchanged in the DMRG calculation with up to $m = 4000$ states kept.

We then study magnetization distributions of the symmetry-breaking phases. For the FM_{U_6} phase, the spin ordering is very similar to what is shown in Eq. (15) but with

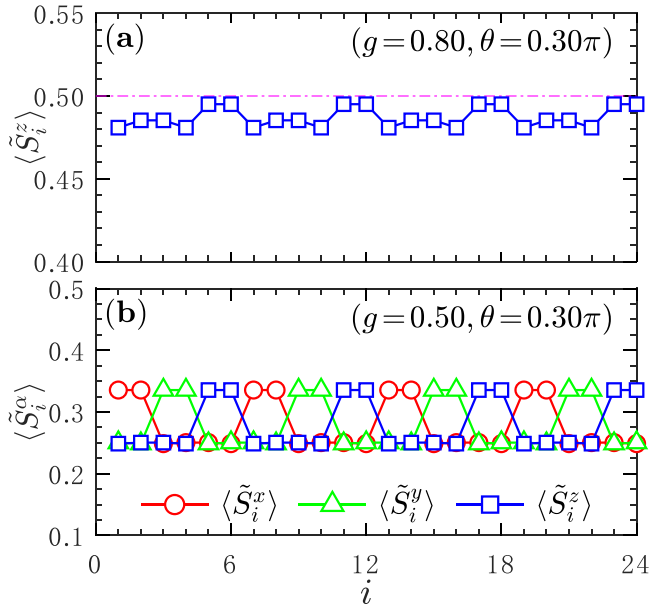

FIG. 9. Local magnetization $\tilde{S}_i^\alpha$ ($\alpha = x, y, z$) as a function of site index i for a 24-site chain. (a) $\tilde{S}_i^z$ in the FM_{U_6} phase at ($g = 0.80$, $\theta = 0.30\pi$). (b) $\tilde{S}_i^x$ (red circles), $\tilde{S}_i^y$ (green triangles), and $\tilde{S}_i^z$ (blue squares) in the M_1 phase at ($g = 0.50$, $\theta = 0.30\pi$).

a six-site periodicity, see Fig. 9(a). It is observed that

$$(\langle\tilde{\mathbf{S}}_1\rangle, \langle\tilde{\mathbf{S}}_2\rangle, \langle\tilde{\mathbf{S}}_3\rangle; \langle\tilde{\mathbf{S}}_4\rangle, \langle\tilde{\mathbf{S}}_5\rangle, \langle\tilde{\mathbf{S}}_6\rangle) = (c, b, b; c, a, a)\hat{z}, \quad (16)$$

where a, b, and c are the magnitudes of the spin orderings along the $\hat{z}$ direction and $a, b, c \leqslant S$. There is a slight difference between a and b when $g \neq 1$. That is, $b < a$ ($b > a$) when $g < 1$ ($g > 1$). They are equal at the isotropic case, consistent with the group-theoretical argument [17]. As can be seen from Fig. 9(a), c is the smallest value of the three, albeit its difference to the penultimate value (it is b when $g < 1$) becomes negligible as g is decreased. For the M_1 phase shown in Fig. 9(b), the z component of the magnetization still shows the pattern in Eq. (16), except that c and b are very close in value but are visibly smaller than a. Most importantly, the x and y components of the spins in the M_1 phase also become nonzero and shows the permutation relation within each even and odd sublattice. Following the η notation of Rousochatzakis and Perkins [63], we find that

$$\langle\tilde{\mathbf{S}}_1\rangle = \begin{pmatrix}\eta_x a\\ \eta_y b\\ \eta_z c\end{pmatrix}, \quad \langle\tilde{\mathbf{S}}_3\rangle = \begin{pmatrix}\eta_x c\\ \eta_y a\\ \eta_z b\end{pmatrix}, \quad \langle\tilde{\mathbf{S}}_5\rangle = \begin{pmatrix}\eta_x b\\ \eta_y c\\ \eta_z a\end{pmatrix} \quad (17)$$

and

$$\langle\tilde{\mathbf{S}}_2\rangle = \begin{pmatrix}\eta_x a\\ \eta_y c\\ \eta_z b\end{pmatrix}, \quad \langle\tilde{\mathbf{S}}_4\rangle = \begin{pmatrix}\eta_x b\\ \eta_y a\\ \eta_z c\end{pmatrix}, \quad \langle\tilde{\mathbf{S}}_6\rangle = \begin{pmatrix}\eta_x c\\ \eta_y b\\ \eta_z a\end{pmatrix}. \quad (18)$$

Here, a, b, c ($\geqslant 0$) are the intensities of the magnetization, while η_x, η_y, η_z ($= \pm 1$) are the Ising variables. It is worth noting that a, b, and c in the M_1 phase satisfy the restriction $(a^2 + b^2 + c^2)^{1/2} \leqslant S$, and it is quite different from these in the FM_{U_6} phase [see Eq. (16)]. All the three η are free to choose either 1 or -1, accounting for the eightfold degeneracy of the M_1 phase shown in Fig. 8. In addition, by applying the

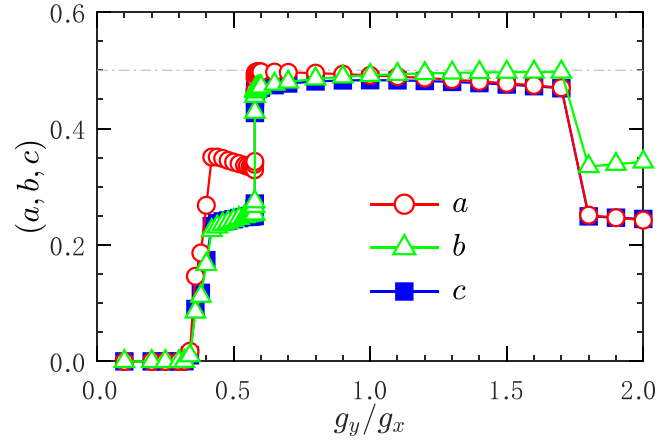

FIG. 10. The a (red circles), b (green triangles), and c (blue squares) magnetization components of the FM_{U_6} and M_1 phases for $\theta = 0.30\pi$ with chain length $L = 48$. The middle region is the FM_{U_6} phase ($0.5778 \lesssim g \lesssim 1.731$) while the side ones are the self-dual M_1 phases.

inversion U_6 transformation, the spins in the original basis have the following relation: $(|S_\upsilon^x|, |S_\upsilon^y|, |S_\upsilon^z|) = (a, b, c)$ for $1 \leqslant \upsilon \leqslant L$. The spin structure of the M_1 phase is noncoplanar in the rotated basis and it could be verified by the scalar spin chirality defined as

$$\hat{\chi}_{ijk} = \tilde{\mathbf{S}}_i \cdot (\tilde{\mathbf{S}}_j \times \tilde{\mathbf{S}}_k). \quad (19)$$

It is easy to check that $\hat{\chi}_{135} = \hat{\chi}_{246} \equiv \hat{\chi}_0$ and

$$\begin{aligned}\hat{\chi}_0 &= \eta_x\eta_y\eta_z(a^3 + b^3 + c^3 - 3abc)\\ &= \frac{\eta}{2}(a + b + c)[(a - b)^2 + (b - c)^2 + (c - a)^2], \end{aligned} \quad (20)$$

with $\eta \equiv \eta_x\eta_y\eta_z$. Equation (20) suggests that, as long as a, b, and c are not all the same, which always holds as observed from Fig. 9(b), $\hat{\chi}_0$ will be nonzero, in line with the noncoplanar pattern of the M_1 phase.

Figure 10 shows the (a, b, c) components of the magnetization along the line of $\theta = 0.30\pi$. In the wide region of $0.5778 \lesssim g \lesssim 1.731$, the ground state is the FM_{U_6} phase where all the spins point along the z direction with an almost-saturated moment. The three species a, b, and c are totally different as long as $g \neq 1$. The M_1 phase takes over when $0.43 < g < 0.5778$, and magnitudes of the magnetization are suppressed approximately to 3/4 (for a) or $\frac{1}{2}$ (for b, c) of the saturated value.

For the M_2 phase, the local magnetization is fragile and we thus extract their values by calculating the spin-spin correlation functions defined as

$$C_\upsilon^\alpha(l) = \langle\tilde{S}_\upsilon^\alpha \tilde{S}_{\upsilon+l}^\alpha\rangle, \quad (21)$$

where $\alpha = x, y, z$ and υ is the reference site. For simplicity we first consider the isotropic case ($g = 1$) which shows a three-site periodicity in the rotated basis. The correlators $C^{x/y/z}$ at ($g = 1.00$, $\theta = 0.42\pi$) are calculated based on a 48-site chain, see Fig. 11. These values are very stable when the site distance l is larger than 10, and we estimate the local magnetization as $\langle\tilde{S}_\upsilon^\alpha\rangle = [C_\upsilon^\alpha(L/2)]^{1/2}$ with $L = 48$. The local magnetization $\langle\tilde{\mathbf{S}}_\upsilon\rangle = (\langle\tilde{S}_\upsilon^x\rangle, \langle\tilde{S}_\upsilon^y\rangle, \langle\tilde{S}_\upsilon^z\rangle)^T$ within the three-site

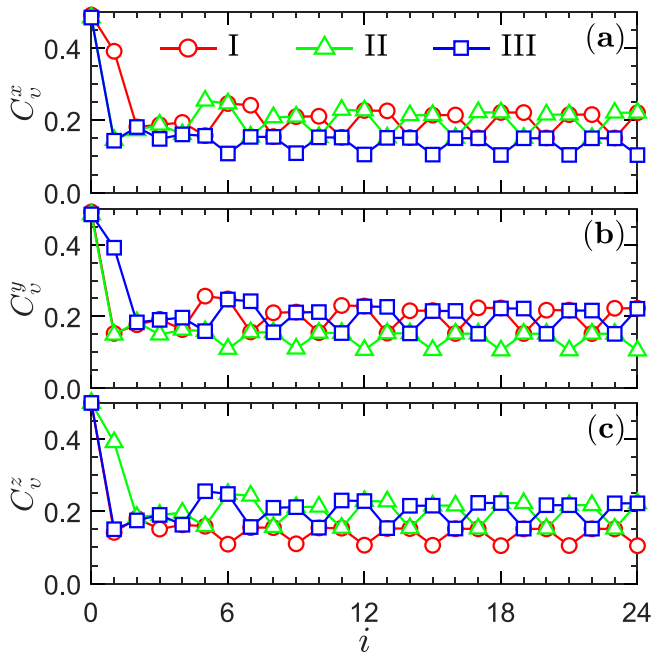

FIG. 11. Spin correlators C_υ^α ($\alpha = x, y, z$) of a segment l for a 48-site chain. The reference site υ could be I (site 1), II (site 2), III (site 3). Panels (a)–(c) are for C^x, C^y, and C^z in the M_2 phase at ($g = 1.00, \theta = 0.42\pi$), respectively.

unit cell is

$$(\langle\tilde{\mathbf{S}}_1\rangle, \langle\tilde{\mathbf{S}}_2\rangle, \langle\tilde{\mathbf{S}}_3\rangle) = \left(\begin{bmatrix}0.214\\0.214\\0.103\end{bmatrix}, \begin{bmatrix}0.214\\0.103\\0.214\end{bmatrix}, \begin{bmatrix}0.103\\0.214\\0.214\end{bmatrix}\right).$$

When away from the isotropic line where $g = 1$, the unit cell is doubled and there is a same magnetization distribution to that one shown in Eqs. (17) and (18). It should be noted that both M_1 and M_2 phases are eightfold degenerate and their difference lies in the relative values among a, b, and c. For M_1 phase we have $c \simeq b < a$ (when $g < 1$) or $c \simeq a < b$ (when $g > 1$), while for M_2 phase c is much smaller than a, b.

B. Magnetic orderings of M_1 and M_2 phases

This section is devoted to study the transitions to M_1 and M_2 phases. We begin by considering the transitions to M_1 phase along the path of $g = 0.5$. The SOPs of the Haldane-type $\mathcal{O}_H = \mathcal{O}_e^z$ [via Eq. (6)] and the Kitaev-type $\mathcal{O}_K = \mathcal{O}_K^x$ [via Eq. (2)] are plotted in Fig. 12(a). At $\theta_H \approx 0.215\pi$ and $\theta_K \approx 0.383\pi$, the two SOPs are discontinuous, indicating of first-order transitions between the EH (A_x) phase and the intermediate M_1 phase. The order parameter O_{M_1} is shown in Fig. 12(b). Here, only the c flavor of $\langle S_i^z\rangle$ is chosen for the sake of brevity. We find that it is very robust with a negligible finite-size effects. In addition, there is also a nonvanishing correlation of a rank-two spin-nematic (SN) ordering defined in Eq. (23) (not shown). Notably, when crossing the line of $\theta = \pi/4$ where the ground state is the SU(2) FM phase, O_{M_1} has a discontinuity because of the inherent difference of the spin orientations.

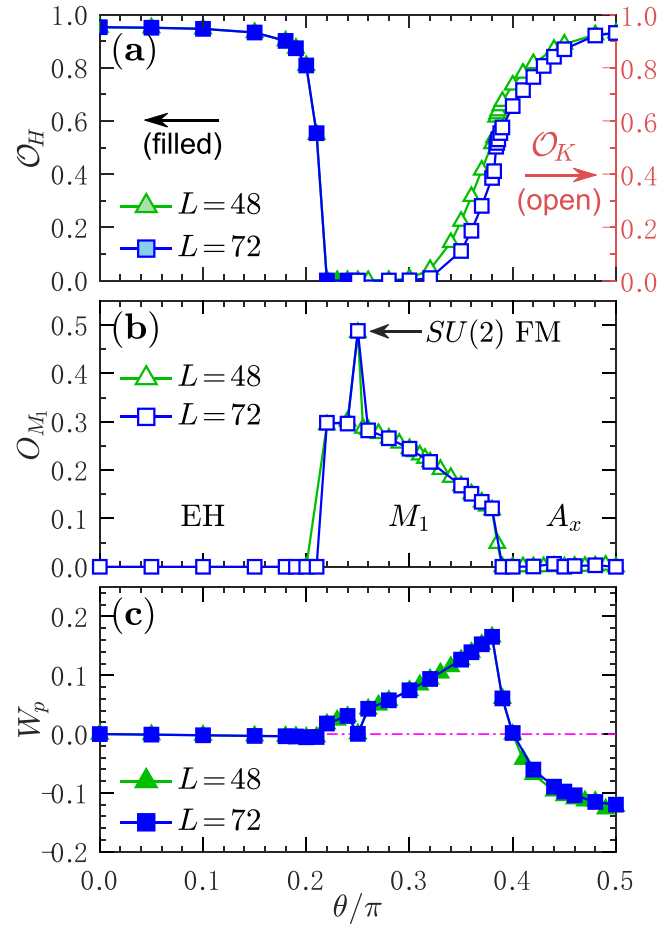

FIG. 12. (a) SOPs of the Haldane-type $\mathcal{O}_H$ (filled symbols) and Kitaev-type $\mathcal{O}_K$ (open symbols) for $g = 0.5$ with chain length $L = 48$ (green triangles) and 72 (blue squares). (b) Order parameter of the M_1 phase O_{M_1} (c component only) and (c) flux density $\langle W_p\rangle$ in the same region as in panel (a).

Meanwhile, it is appealing to know how the flux density $\langle\hat{W}_p\rangle$,

$$\hat{W}_p = 2^6\tilde{S}_1^z\tilde{S}_2^y\tilde{S}_3^x\tilde{S}_4^z\tilde{S}_5^y\tilde{S}_6^x, \tag{22}$$

evolves in each different phase. Similar to the two-dimensional counterpart [2], the quantity in Eq. (22) is the product of spin operators on consecutive overhanging bonds within the six-site unit cell [see Fig. 1(b)]. In Fig. 12(c), we plot the flux density $\langle\hat{W}_p\rangle$ versus θ in the whole region of $\theta \in [0, \pi/2]$. It is clearly shown that $\langle\hat{W}_p\rangle$ is zero in the EH phase. In the M_1 phase, $\langle\hat{W}_p\rangle$ starts from a nonzero value and goes up with the increasing of θ except for $\theta = \pi/4$ where $\langle\hat{W}_p\rangle \simeq 0$. In the A_x phase, however, $\langle\hat{W}_p\rangle$ decreases from 0.17 or so and does not stop dropping until $\theta \simeq 0.50$ where $\langle\hat{W}_p\rangle < 0$. Without doubt, the flux density $\langle\hat{W}_p\rangle$ shows a crucial difference among the three distinct phases. The jump and kink are excellent probes for phase transitions involved.

We now turn to the transition around the M_2 phase. It is shown in the isotropic K-Γ chain that there is an intermediate phase when $0.40\pi \lesssim \theta \lesssim 0.466\pi$ [18]. This phase is now recognized as the M_2 phase with a nonzero magnetization, and it could survive against small anisotropy where $|g - 1| \ll 1$,

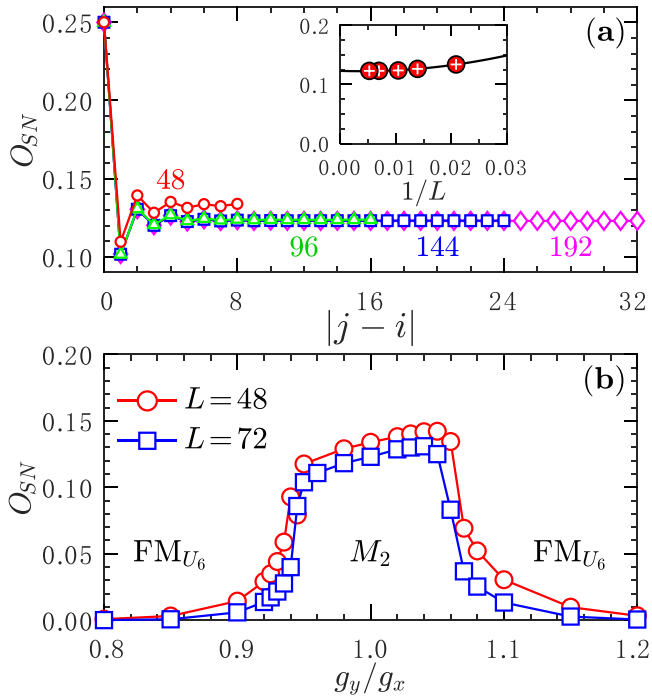

FIG. 13. (a) Correlations of the SN order [see Eq. (23)] for chain length $L = 48$, 96, 144, and 192. The selected point at ($g = 1.00$, $\theta = 0.42\pi$) is deep in the M_2 phase. Inset shows the extrapolation of the SN order to infinite-size system. (b) Order parameter O_{SN} of the M_2 phase for $\theta = 0.42\pi$ with chain length $L = 48$ (red circles) and 72 (blue squares).

and then gives way to the conventional collinear FM_{U_6} phase. Although both phases are magnetically ordered, we appreciate the rank-two SN ordering as a sensitive probe to capture the phase transition. It is finite in the M_2 phase while vanishes in the FM_{U_6} phase since the latter is collinear. The SN correlation function in the long-distance limit is known as [18]

$$O_{SN}^2 = \lim_{|j-i|\gg 1} \langle \tilde{S}^y_{3i+1}\tilde{S}^z_{3i+2} \cdot \tilde{S}^y_{3j+1}\tilde{S}^z_{3j+2}\rangle. \tag{23}$$

Since the species of spins in the correlator of Eq. (23) always come in pairs, the sign of the correlation remains uninfluenced. In addition, on can infer from Eqs. (17) and (18) that there is no difference of the magnetization among the degenerate ground states, indicating that all of them will produce a same value of the order parameter. As a result, we do not need to distinguish these states and the value of the order parameter could be safely obtained via Eq. (23).

Figure 13 shows the order parameter O_{SN} for $\theta = 0.42\pi$. To check for the finite-size effect, we consider the isotropic case $g = 1$ and calculate the correlation function in Eq. (23) with $i = 0$ and $j = 0, 1, 2, \ldots, L/6$, see Fig. 13(a). It is found that the correlators saturate to a finite value after several times of oscillation. In what follows we shall define $O_{SN} \equiv O_{SN}(i = 0, j = L/6)$. The inset shows the extrapolation of the SN order parameter for chain length $L = 48$, 72, 96, 144, and 192, from which we can clearly find that O_{SN} is very robust against L. We then extend the calculation of O_{SN} for $0.8 \leqslant g \leqslant 1.2$ and the results are summarized in Fig. 13(b). Deep into the M_2 phase, O_{SN} is very stable, although there is a modest suppression near the boundaries. The transitions between the M_2 phase and the collinear FM_{U_6} phase are accompanied by the jumps of O_{SN}, from which the transition points are determined as $g_t \approx 0.945$ and 1.065, respectively. It is worth mentioning that the transition points satisfy the self-dual relation shown in Eq. (3) since they are related as $0.945 \simeq 1/1.065$.

Empirically, the ground-state energy per-site of the FM_{U_6} phase is given by

$$e_g^{\mathrm{FM}_{U_6}} = -\tfrac{1}{6}[K(a^2 + gb^2) + 2c\Gamma(b + ga)], \tag{24}$$

where a, b, c are almost saturated [see Figs. 9(a) and 10]. For example, at the hidden SU(2) FM point where $K = \Gamma$ and $g = 1$, we have $a = b = c = \frac{1}{2}$ and the energy inferred from Eq. (24) is $-K/4$, consistent with the analytical result [61]. For the M_2 (and also M_1) phase, the energy displays a very similar form except that the prefactor ($\frac{1}{6}$) in Eq. (24) should be $\frac{1}{2}$. In addition, (a, b, c) is subject to the constraint $\overline{M} \equiv (a^2 + b^2 + c^2)^{1/2} \leqslant S$. However, the total magnetization $\overline{M}$ of the M_2 phase is far from saturated, and it is only 0.320 with $(a, b, c) = (0.214, 0.214, 0.103)$ at ($g = 1.00$, $\theta = 0.42\pi$). By adding the bond alternation with $g \neq 1$, there is a slight enhancement of $\overline{M}$, lowering the ground-state energy and thus opening a finite region of M_2 phase.

VI. TRANSITIONS AROUND THE FERROMAGNETIC KITAEV LIMIT

So far, we have mainly concentrated on the right panel of the phase diagram shown in Fig. 2. Phases in the left panel could be obtained from the right part after a mirror operation. However, little is known about the transition types of the adjacent phases near the axis of symmetry. After an inspection of the first-order energy derivative $\partial e_g/\partial\theta$ along the line of $g = 1$, Yang *et al.* claimed that the transition at the FM Kitaev point is of first order [17]. A variational Monte Carlo study, amazingly, suggests that the Z_2 QSL at that point could survive up to a small Γ interaction [64]. Herein, we find that the FM Kitaev point is a confluence point of two transition lines, i.e., the A_x-A_y and the LL-LL′ transition lines. It is thus a multicritical point which accounts for the difficulty in determining the nature of transition (for an extended discussion, see Sec. III in the Supplemental Material [36]). By virtue of an efficient bond-reversal method [65], we argue in the following that the aforesaid topological QPT between the two LLs is continuous. Nevertheless, away from the symmetric line of $g = 1$, transitions at $\theta = -\pi/2$ are of first order without closing the gap at the transition points.

Here we illustrate how to use the bond-reversal method to determine the transition type around the FM Kitaev point. By tuning Γ from negative to positive, the ground-state energy e_g must be symmetric with respect to the $\Gamma = 0$ line (i.e., $\theta = -\pi/2$) due to the symmetry relation of Eq. (4). When θ is slightly away from $-\pi/2$, the sign of the Γ interaction is changed, and local expectations of $\Gamma_x = \langle S^y_1 S^z_2 + S^z_1 S^y_2\rangle$ and $\Gamma_y = \langle S^z_2 S^x_3 + S^x_2 S^z_3\rangle$ in the *original* basis must be reversed. In this regard, we thus define the difference of bond strength (DBS) $\mathcal{D}$ as

$$\mathcal{D} = \tfrac{1}{2}(\Gamma_x + \Gamma_y). \tag{25}$$

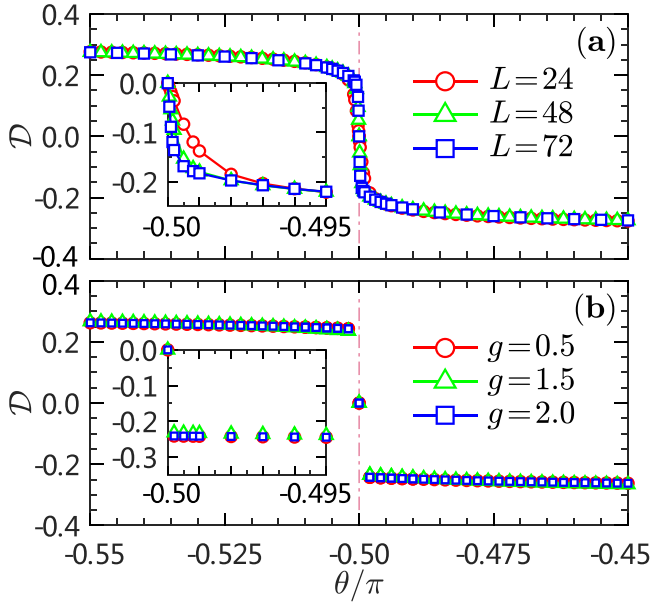

FIG. 14. (a) DBS $\mathcal{D}$ of the g_x-g_y K-Γ chain for $g = 1.0$ with chain length $L = 24$ (red circles), 48 (green triangles) and 72 (blue squares). Inset shows a zoom-in of the DBS near the FM Kitaev limit with $\Gamma > 0$. (b) DBS $\mathcal{D}$ for $g = 0.5$ (red circles), 1.5 (green triangles) and 2.0 (blue squares) with chain length $L = 24$.

The DBS $\mathcal{D}$ is a sensitive probe for a first-order QPT because it has a jump at the transition point. Oppositely, there is a continuous QPT if $\mathcal{D}$ is smoothly changed [65]. We note in passing that, physically, $\mathcal{D}$ is equivalent to the first-order derivative of ground-state energy $\partial e_g/\partial\theta$ when $g = 1$. However, the energy derivative depends on the increment $\delta\theta$ which may cause artificial oscillation. In this sense, the DBS $\mathcal{D}$ is obviously superior and is more reliable.

Figure 14(a) shows the DBS $\mathcal{D}$ of the LL-LL′ transition when $g = 1.0$. It is rather smooth without any jump in a wide region of $-0.55\pi \leqslant \theta \leqslant -0.45\pi$. The size-dependent behavior is insignificant except for a narrow slit near the FM Kitaev point. As can be seen from the inset of Fig. 14(a), the DBS $\mathcal{D}$ shows a well-controlled scaling behavior for different chain length L and does not have a jump although its slope becomes sharp as L increases, indicative of a multicritical behavior. We recall that such a multicritical point is analogous to the one existing in a 1D transverse XY spin chain which owns an intersection point of two transition lines of different universality classes [66–68]. When shifting away from $g = 1.0$, the ground state is occupied by gapped EH or OH phase. The DBS $\mathcal{D}$ for three selected EH-EH′ transition ($g = 0.5$) and OH-OH′ transitions ($g = 1.5$ and 2.0) are shown in Fig. 14(b). For all the cases there are appreciable jumps of $\mathcal{D}$ at $\theta = -\pi/2$, representing the hallmark character of the first-order QPT.

VII. SUMMARY AND DISCUSSION

We have numerically studied the phases and phase transitions in a bond-alternating spin-$\frac{1}{2}$ K-Γ chain, which is an excellent platform to reveal many aspects of one-dimensional quantum magnetism. By calculating various conventional symmetry-breaking order parameters and nonlocal SOPs, we unveil a rich quantum phase diagram which contains seven different phases. Near the AFM Kitaev spin chain limit, there is a critical segment with a macroscopic ground-state degeneracy. It is unstable against bond alternation, resulting in two gapped disordered A_x and A_y phases characterized by nonlocal SOPs. The A_x-A_y topological QPT falls in the Ising universality class with a central charge $c = \frac{1}{2}$. On the other hand, starting from the FM Kitaev spin chain limit by increasing the Γ interaction, there are EH and OH phases in the inner circle ($g < 1$) and outer circle ($g < 1$), respectively. The EH-OH transition is determined by the SOPs which vanish algebraically at the transition boundary. It could also be captured by the entanglement gap which undergoes a sign change when crossing the critical point. This transition belongs to the Gaussian universality class with a central charge $c = 1$, identical to that of the bond-alternating spin-$\frac{1}{2}$ AFM Heisenberg chain. The FM Kitaev point is recognized as a multicritical point converging several different phases. In addition, there are also three distinct magnetically ordered states, named FM_{U_6}, M_1, and M_2 phases, in the presence of AFM Kitaev interaction. The FM_{U_6} phase has a sixfold degeneracy and is situated in a wide region around the isotropic line of $g = 1$. The M_1 and M_2 phases are highly spatially modulated and could have a rank-two spin-nematic ordering.

The isotropic Γ chain is conformally invariant with a central charge $c = 1$. While its ground-state energy smoothly varies with the chain length under OBC, it surprisingly shows an unconventional six-site periodicity under PBC. We remark that this phenomenon has a profound relation to the abnormal energy scaling in two-dimensional honeycomb lattice [15]. Given that there is an emergent SU(2) symmetry at this Γ limit [17], we conjecture that the versatile Bethe ansatz may be capable to give an exact solution of the isotropic Γ chain.

In closing, our work demonstrates the essential role played by the bond alternation in enriching the underlying phase diagram. The bond alternation is a relevant perturbation to either open up the energy gap or rearrange the distribution of magnetization, leaving the possibility for the emergence of novel phases. Our study also highlights the richness of Kitaev systems with AFM exchange interaction. Although the K-Γ model is widely recognized as a cornerstone to describe candidate Kitaev materials like α-$RuCl_3$, much less attention has been paid to $K > 0$ as Kitaev interaction is likely negative in these materials. A theoretical proposal for the AFM Kitaev interaction in f-electron-based magnets has been proposed [69]. Our study thus corroborates a new direction to hunt for exotic phases in a less explored area.

ACKNOWLEDGMENTS

Q.L. would like to thank W.-L. You for fruitful discussions on the quantum compass model. X.W. was supported by the National Program on Key Research Project (Grant No. 2016YFA0300501) and the National Natural Science Foundation of China (Grant No. 11974244), He also acknowledged the support from a Shanghai talent program. J.Z. was supported by the National Natural Science Foundation of China (Grant No. 11874188). H.-Y.K. was supported by the NSERC Discovery Grant No. 06089-2016, the Centre for Quantum Materials at the University of Toronto, the

Canadian Institute for Advanced Research, and also a funding from the Canada Research Chairs Program. Computations at early stages were performed on the Tianhe-2JK at the Beijing Computational Science Research Center (CSRC). Computations were mostly performed on the Niagara supercomputer at the SciNet HPC Consortium. SciNet is funded by the Canada Foundation for Innovation under the auspices of Compute Canada; the Government of Ontario; Ontario Research Fund - Research Excellence; and the University of Toronto.

[1] P. W. Anderson, Mater. Res. Bull. **8**, 153 (1973).
[2] A. Kitaev, Ann. Phys. (NY) **321**, 2 (2006).
[3] G. Jackeli and G. Khaliullin, Phys. Rev. Lett. **102**, 017205 (2009).
[4] J. G. Rau, E. K.-H. Lee, and H.-Y. Kee, Annu. Rev. Condens. Matter Phys. **7**, 195 (2016).
[5] H. Takagi, T. Takayama, G. Jackeli, G. Khaliullin, and S. E. Nagler, Nat. Rev. Phys. **1**, 264 (2019).
[6] J. G. Rau, Eric Kin-Ho Lee, and H.-Y. Kee, Phys. Rev. Lett. **112**, 077204 (2014).
[7] X. Liu, T. Berlijn, W.-G. Yin, W. Ku, A. Tsvelik, Young-June Kim, H. Gretarsson, Yogesh Singh, P. Gegenwart, and J. P. Hill, Phys. Rev. B **83**, 220403(R) (2011).
[8] J. Chaloupka, G. Jackeli, and G. Khaliullin, Phys. Rev. Lett. **110**, 097204 (2013).
[9] K. W. Plumb, J. P. Clancy, L. J. Sandilands, V. V. Shankar, Y. F. Hu, K. S. Burch, H.-Y. Kee, and Y.-J. Kim, Phys. Rev. B **90**, 041112(R) (2014).
[10] R. D. Johnson, S. C. Williams, A. A. Haghighirad, J. Singleton, V. Zapf, P. Manuel, I. I. Mazin, Y. Li, H. O. Jeschke, R. Valentí, and R. Coldea, Phys. Rev. B **92**, 235119 (2015).
[11] W. Wang, Z.-Y. Dong, S.-L. Yu, and J.-X. Li, Phys. Rev. B **96**, 115103 (2017).
[12] A. Catuneanu, Y. Yamaji, G. Wachtel, Y.-B. Kim, and H.-Y. Kee, npj Quantum Mater. **3**, 23 (2018).
[13] M. Gohlke, G. Wachtel, Y. Yamaji, F. Pollmann, and Y. B. Kim, Phys. Rev. B **97**, 075126 (2018).
[14] J. Wang, B. Normand, and Z.-X. Liu, Phys. Rev. Lett. **123**, 197201 (2019).
[15] Q. Luo, J. Zhao, H.-Y. Kee, and X. Wang, arXiv:1910.01562.
[16] T. Yamada, T. Suzuki, and S.-I. Suga, Phys. Rev. B **102**, 024415 (2020).
[17] W. Yang, A. Nocera, T. Tummuru, H.-Y. Kee, and I. Affleck, Phys. Rev. Lett. **124**, 147205 (2020).
[18] W. Yang, A. Nocera, E. S. Sørensen, H.-Y. Kee, and I. Affleck, Phys. Rev. B **103**, 054437 (2021).
[19] W. Yang, A. Nocera, and I. Affleck, Phys. Rev. Research **2**, 033268 (2020).
[20] E. S. Sørensen, A. Catuneanu, J. S. Gordon, and H.-Y. Kee, Phys. Rev. X **11**, 011013 (2021).
[21] S. Sachdev, *Quantum Phase Transitions* (Cambridge University Press, Cambridge, 2011).
[22] J. M. Kosterlitz and D. J. Thouless, J. Phys. C: Solid State Phys. **6**, 1181 (1973).
[23] D. C. Tsui, H. L. Stormer, and A. C. Gossard, Phys. Rev. Lett. **48**, 1559 (1982).
[24] F. D. M. Haldane, Phys. Rev. Lett. **50**, 1153 (1983).
[25] X. G. Wen, Rev. Mod. Phys. **89**, 041004 (2017).
[26] F. Pollmann, E. Berg, A. M. Turner, and M. Oshikawa, Phys. Rev. B **85**, 075125 (2012).
[27] M. den Nijs and K. Rommelse, Phys. Rev. B **40**, 4709 (1989).
[28] T. Kennedy and H. Tasaki, Phys. Rev. B **45**, 304 (1992).
[29] K. Hida, Phys. Rev. B **45**, 2207 (1992).
[30] X. Chen, Z.-C. Gu, and X.-G. Wen, Phys. Rev. B **83**, 035107 (2011).
[31] W. Brzezicki, J. Dziarmaga, and A. M. Oleś, Phys. Rev. B **75**, 134415 (2007).
[32] W.-L. You and G.-S. Tian, Phys. Rev. B **78**, 184406 (2008).
[33] S. R. White, Phys. Rev. Lett. **69**, 2863 (1992).
[34] I. Peschel, X. Q. Wang, M. Kaulke, and K. Hallberg, *Density-Matrix Renormalization* (Springer, Berlin, 1999).
[35] U. Schollwöck, Rev. Mod. Phys. **77**, 259 (2005).
[36] See Supplemental Material at http://link.aps.org/supplemental/10.1103/PhysRevB.103.144423 for the exact solution of the Kitaev spin chain, the QPT of the bond-alternating Heisenberg chain, and multicritical point of the FM Kitaev point.
[37] P. Pfeuty, Ann. Phys. (NY) **57**, 79 (1970).
[38] T. Barnes, J. Riera, and D. A. Tennant, Phys. Rev. B **59**, 11384 (1999).
[39] D. C. Johnston, R. K. Kremer, M. Troyer, X. Wang, A. Klümper, S. L. Bud'ko, A. F. Panchula, and P. C. Canfield, Phys. Rev. B **61**, 9558 (2000).
[40] H. T. Wang, B. Li, and S. Y. Cho, Phys. Rev. B **87**, 054402 (2013).
[41] R. Haghshenas, A. Langari, and A. T. Rezakhani, J. Phys.: Condens. Matter **26**, 456001 (2014).
[42] M. Bortz, J. Sato, and M. Shiroishi, J. Phys. A: Math. Theor. **40**, 4253 (2007).
[43] F. Pollmann, A. M. Turner, E. Berg, and M. Oshikawa, Phys. Rev. B **81**, 064439 (2010).
[44] C. Tan, H. Saleur, and S. Haas, Phys. Rev. B **101**, 235155 (2020).
[45] G. Vidal, J. I. Latorre, E. Rico, and A. Kitaev, Phys. Rev. Lett. **90**, 227902 (2003).
[46] Z.-A. Liu, T.-C. Yi, J.-H. Sun, Y.-L. Dong, and W.-L. You, Phys. Rev. E **102**, 032127 (2020).
[47] H. W. J. Blöte, J. L. Cardy, and M. P. Nightingale, Phys. Rev. Lett. **56**, 742 (1986).
[48] I. Affleck, Phys. Rev. Lett. **56**, 746 (1986).
[49] Z. Nussinov and J. van den Brink, Rev. Mod. Phys. **87**, 1 (2015).
[50] X.-Y. Feng, G.-M. Zhang, and T. Xiang, Phys. Rev. Lett. **98**, 087204 (2007).
[51] K.-W. Sun and Q.-H. Chen, Phys. Rev. B **80**, 174417 (2009).
[52] V. Subrahmanyam, Phys. Rev. A **88**, 032315 (2013).
[53] W.-L. You, Y. Wang, T.-C. Yi, C. Zhang, and A. M. Oleś, Phys. Rev. B **97**, 224420 (2018).
[54] V. K. Vimal and V. Subrahmanyam, Phys. Rev. A **98**, 052303 (2018).
[55] N. Wu and W.-L. You, Phys. Rev. B **100**, 085130 (2019).
[56] R. Steinigeweg and W. Brenig, Phys. Rev. B **93**, 214425 (2016).
[57] N. Shibata and H. Katsura, Phys. Rev. B **99**, 174303 (2019).

[58] A. Catuneanu, E. S. Sórensen, and H.-Y. Kee, Phys. Rev. B **99**, 195112 (2019).
[59] H. T. Wang and S. Y. Cho, J. Phys.: Condens. Matter **27**, 015603 (2015).
[60] F. Yang, K. Plekhanov, and K. Le Hur, Phys. Rev. Research **2**, 013005 (2020).
[61] T. Koma and B. Nachtergaele, Lett. Math. Phys. **40**, 1 (1997).
[62] P. Chen, Z.-L. Xue, I. P. McCulloch, M.-C. Chung, M. Cazalilla, and S.-K. Yip, J. Stat. Mech. (2013) P10007.
[63] I. Rousochatzakis and N. B. Perkins, Phys. Rev. Lett. **118**, 147204 (2017).
[64] J. Wang and Z.-X. Liu, Phys. Rev. B **102**, 094416 (2020).
[65] Q. Luo, J. Zhao, and X. Wang, Phys. Rev. B **100**, 121111(R) (2019).
[66] E. Lieb, T. Schultz, and D. Mattis, Ann. Phys. (NY) **16**, 407 (1961).
[67] K. Damle and S. Sachdev, Phys. Rev. Lett. **76**, 4412 (1996).
[68] X. M. Yang, G. Zhang, and Z. Song, J. Phys.: Condens. Matter **31**, 245401 (2019).
[69] S.-H. Jang, R. Sano, Y. Kato, and Y. Motome, Phys. Rev. B **99**, 241106(R) (2019).